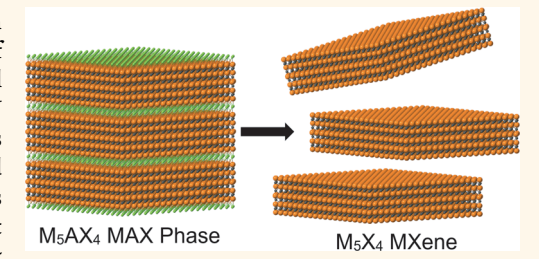
# Synthesis of Mo<sub>4</sub>VAIC<sub>4</sub> MAX Phase and Two-Dimensional Mo<sub>4</sub>VC<sub>4</sub> MXene with Five Atomic **Layers of Transition Metals**

Grayson Deysher, † © Christopher Eugene Shuck, † © Kanit Hantanasirisakul, † © Nathan C. Frey, ‡ O Alexandre C. Foucher, † © Kathleen Maleski, † © Asia Sarycheva, † Vivek B. Shenoy, † Eric A. Stach, † © Babak Anasori,\*,<sup>†,§</sup> and Yury Gogotsi\*,<sup>†</sup>

Supporting Information

Downloaded via UNIV OF PENNSYLVANIA on July 28, 2020 at 20:15:05 (UTC). See https://pubs.acs.org/sharingguidelines for options on how to legitimately share published articles.

ABSTRACT: MXenes are a family of two-dimensional (2D) transition metal carbides, nitrides, and carbonitrides with a general formula of  $M_{n+1}X_nT_x$ , in which two, three, or four atomic layers of a transition metal (M: Ti, Nb, V, Cr, Mo, Ta, etc.) are interleaved with layers of C and/or N (shown as X), and T<sub>x</sub> represents surface termination groups such as -OH, =O, and -F. Here, we report the scalable synthesis and characterization of a MXene with five atomic layers of transition metals (Mo<sub>4</sub>VC<sub>4</sub>T<sub>r</sub>), by synthesizing its Mo<sub>4</sub>VAlC<sub>4</sub> MAX phase precursor that contains no other MAX phase impurities. These phases display twinning at their central M layers which is not present in any other known MAX



phases or MXenes. Transmission electron microscopy and X-ray diffraction were used to examine the structure of both phases. Energy-dispersive X-ray spectroscopy, X-ray photoelectron spectroscopy, Raman spectroscopy, and highresolution scanning transmission electron microscopy with energy-dispersive X-ray spectroscopy were used to study the composition of these materials. Density functional theory calculations indicate that other five transition metal-layer MAX phases (M'<sub>4</sub>M"AlC<sub>4</sub>) may be possible, where M' and M" are two different transition metals. The predicted existence of additional Al-containing MAX phases suggests that more M5C4Tx MXenes can be synthesized. Additionally, we characterized the optical, electronic, and thermal properties of Mo<sub>4</sub>VC<sub>4</sub>T<sub>x</sub>. This study demonstrates the existence of an additional subfamily of M<sub>5</sub>X<sub>4</sub>T<sub>x</sub> MXenes as well as a twinned structure, allowing for a wider range of 2D structures and compositions for more control over properties, which could lead to many different applications.

**KEYWORDS:** MXene, two-dimensional, MAX phase, synthesis, structure, properties

wo-dimensional (2D) materials such as graphene, hexagonal boron nitride, and transition metal dichalcogenides have gained significant attention due to their interesting electronic, photonic, electrochemical, and optical<sup>4</sup> properties. The 2D nature of these materials allows for different applications compared to their bulk counterparts, including applications such as transitors, solar cells, touch screens, biosensors, and lasers. In 2011, MXenes were introduced as a family of 2D materials. 5 MXenes are 2D transition metal carbides and nitrides that have the formula unit  $M_{n+1}X_nT_n$  where M stands for an early transition metal (Ti, Nb, V, Cr, Mo, Ta, etc.), X stands for carbon and/or nitrogen,  $T_x$  represents surface terminations such as -OH, = O, and -F, and n is an integer from 1 to 3. Here, the common notation  $M_{n+1}X_n$  will be used and we do not show the  $T_x$  for brevity. Within the M2X, M3X2, and M4X3 MXene structures that have been previously reported, there are several compositional possibilities including monometal MXenes, ordered double metal MXenes with in-plane and out-of-plane ordering  $((M'M'')_{n+1}X_n)^6$ , divacancy MXenes with the formula unit M<sub>1,33</sub>X<sub>2</sub><sup>7</sup> and solid-solution MXenes containing a mixture of multiple metals in the M sites.8

MXenes have become increasingly studied due to their exceptional properties such as high volumetric capacitance, antibacterial properties, 10 electrochromic behavior, 11,12 high

Received: September 29, 2019 Accepted: December 5, 2019 Published: December 5, 2019

204

Department of Materials Science and Engineering, and A.J. Drexel Nanomaterials Institute, Drexel University, Philadelphia, Pennsylvania 19104, United States

<sup>\*</sup>Department of Materials Science and Engineering, University of Pennsylvania, Philadelphia, Pennsylvania 19104, United States §Department of Mechanical and Energy Engineering, and Integrated Nanosystems Development Institute, Purdue School of Engineering and Technology, Indiana University-Purdue University Indianapolis, Indianapolis, Indiana 46202, United States

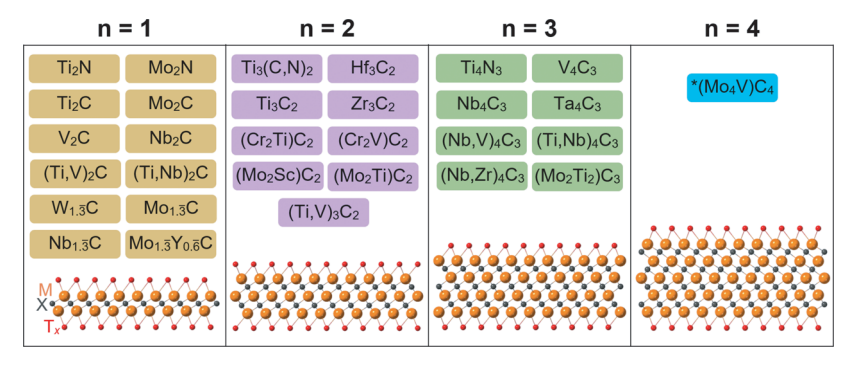


Figure 1. MXenes reported to date. Twelve  $M_2X$  MXenes (n = 1),  $^{7,15,29-36}$  nine  $M_3X_2$  (n = 2),  $^{5,33,37-41}$  and eight  $M_4X_3$  (n = 3),  $^{8,33,37,40,42-44}$  have been synthesized. The MXene reported here is marked by an asterisk (\*). There are also many other MXene compositions that have been theoretically explored  $^{40,45,46}$  and a variety of solid-solutions that have been produced.

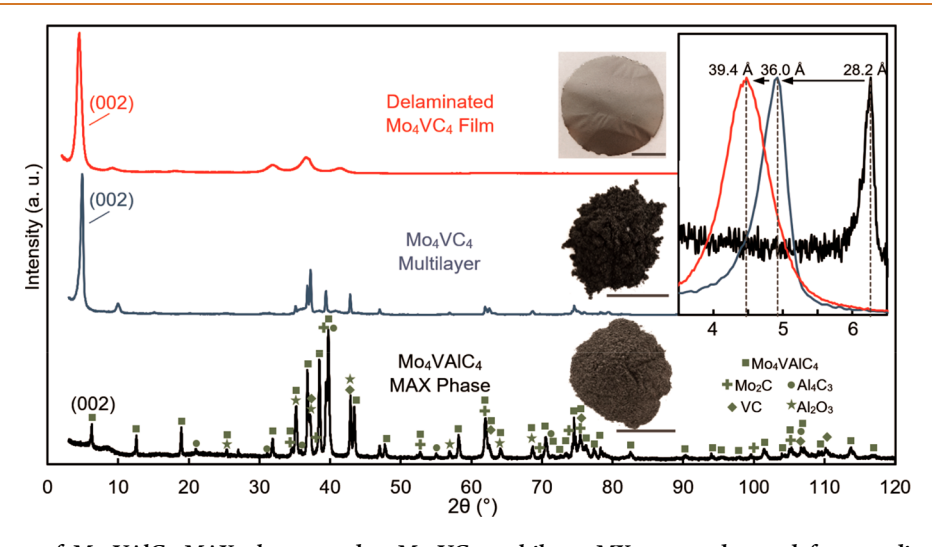


Figure 2. XRD patterns of  $Mo_4VAlC_4$  MAX phase powder,  $Mo_4VC_4$  multilayer MXene powder, and free-standing film of delaminated  $Mo_4VC_4$  MXene. Insets on the top of each XRD pattern show optical images of the corresponding powders/film. The scale bars on the optical images are 1 cm. Top right inset shows a closeup view of the (002) peak shift indicating exfoliation and delamination. The c-LP values are provided for all three XRD patterns at the top of the (002) peaks in the inset.

electronic conductivity, <sup>13</sup> and optical transparency. <sup>14</sup> These properties are beneficial for numerous applications including energy storage, <sup>6,15</sup> catalysis, <sup>16,17</sup> antennas and RFID tags, <sup>18</sup> electromagnetic interference (EMI) shielding, <sup>19,20</sup> sensors, <sup>21</sup> and plasmonic metamaterials. <sup>22</sup> Furthermore, it has been shown that the MXene composition and structure play a vital role in the observed properties. <sup>23–28</sup> A list of MXenes that have been experimentally synthesized and reported in the literature, including the one reported here, is shown in Figure 1.

MXenes are produced by the selective chemical etching of specific atomic planes from layered carbide/nitride precursors. Most commonly,  $M_{n+1}AX_n$  (MAX) phases are the precursor materials and MXenes are produced by selectively etching the A layers, where A represents Al or Si. <sup>6,47</sup> The resulting MXene structure is dependent on its MAX phase precursor, which has limited the MXene family to materials with 2, 3, or 4 atomic layers of transition metal(s). Here, we introduce a MXene with five atomic layers of transition metals ( $M_5X_4$ ) by synthesizing its precursor MAX phase with five atomic layers of transition metals.

Trace impurities of higher order MAX phases (n > 3) have previously been observed including  $Ta_6AlC_5$ , <sup>48</sup> and  $Ti_7SnC_6$ ; <sup>49</sup> however, both have only existed as a secondary component in a mixture with  $M_2AX$  or as intergrown layers in other MAX phases. Similarly to the MAX phase reported here,

 $({
m TiNb})_5 {
m AlC_4}^{50}$  has been synthesized as a  ${
m M_5 AlC_4}$  phase; however, its impurities include  ${
m M_2 AlC}$  and  ${
m M_4 AlC_3}$  MAX phases. The presence of other MAX phases as impurities makes synthesizing a phase pure MXene almost impossible. In general, the presence of different MAX phases ( ${
m M_2 AC}$ , and  ${
m M_4 AC_3}$ ) as impurities results in a mixture of MXene (for example,  ${
m M_2 C}$  and  ${
m M_4 C_3}$  in a  ${
m M_5 C_4}$  MXene). Furthermore, due to similar MXene densities and their 2D nature, separating the resulting mixed MXenes is challenging. Therefore, a  ${
m M_5 AX_4}$  MAX phase with no other MAX phase impurities is required to synthesize phase pure  ${
m M_5 X_4}$  MXene.

Here we present  $\mathrm{Mo_4VAlC_4}$  MAX phase with no other MAX phase impurities, allowing for the synthesis of sufficiently phase pure  $\mathrm{Mo_4VC_4}$  MXene. We provide structural characterization by high-resolution scanning transmission electron microscopy (HR-STEM), X-ray diffraction (XRD), scanning electron microscopy (SEM), and atomic force microscopy (AFM). In addition, chemical characterization by energy-dispersive X-ray spectroscopy (EDS) and X-ray photoelectron spectroscopy (XPS) is presented, with the optical, electrical, and thermal stability properties of  $\mathrm{Mo_4VC_4}$  determined with UV-vis-NIR spectrophotometry, temperature-dependent resistivity, and thermogravimetric analysis (TGA), respectively. Density functional theory (DFT) calculations were used to show the theoretical stabilities of other  $\mathrm{M_5AX_4}$  phases. The scalable

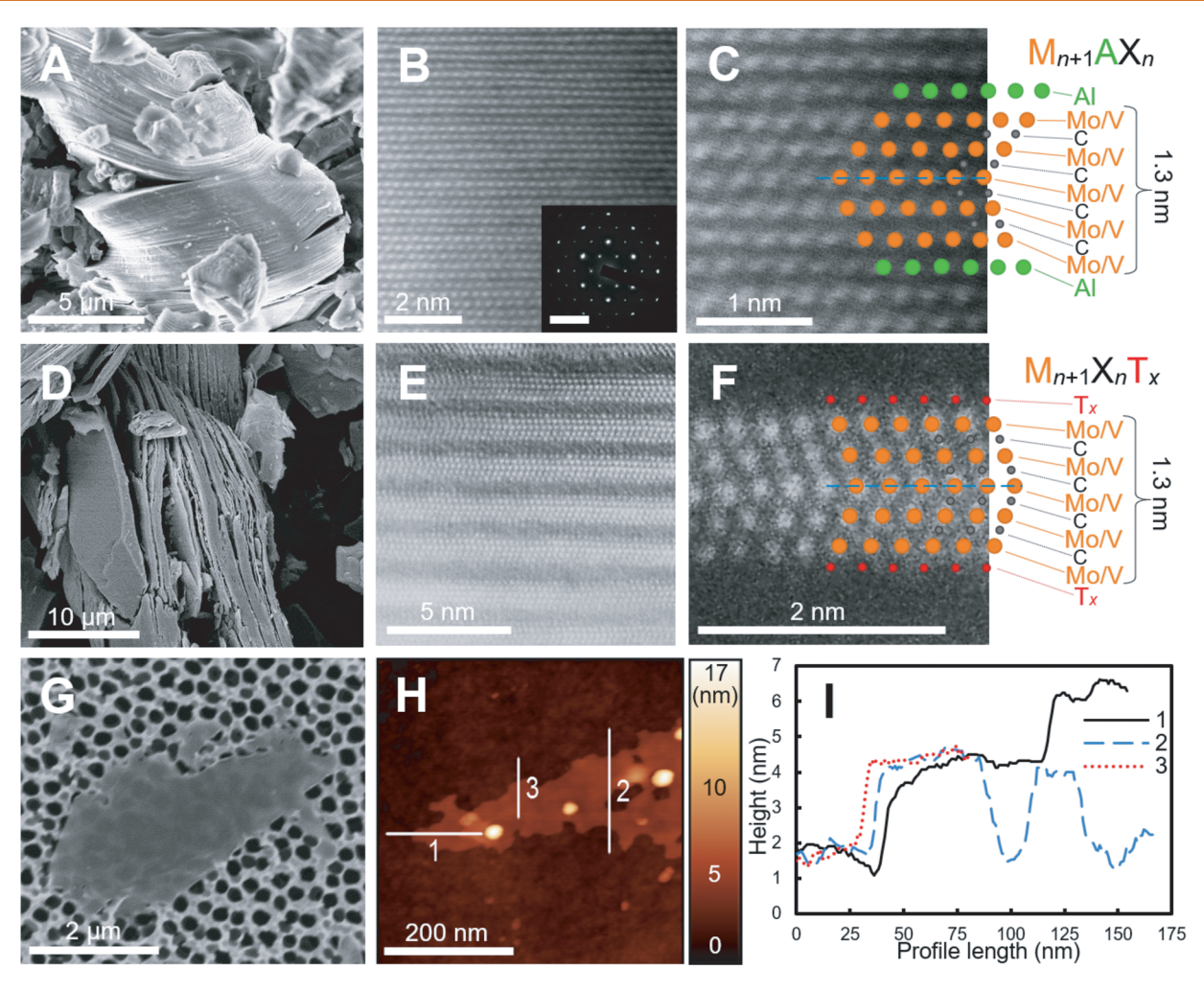


Figure 3. Microscopic analysis of MAX and MXene. (A) SEM micrograph of  $Mo_4VAlC_4$  MAX phase powder. (B) Atomic-resolution dark field STEM micrograph of  $Mo_4VAlC_4$  MAX phase with inset SAED pattern of the [001] zone axis. The scale bar for the SAED pattern is 1 Å<sup>-1</sup>. (C) Dark field STEM micrograph of  $Mo_4VAlC_4$  MAX phase. The solid circles on the right represent the atoms. (D) SEM micrograph of  $Mo_4VC_4$  multilayer MXene powder showing stacked 2D flakes with 5 layers of bright atoms ( $Mo_4VVC_4$  layers). (F) Dark field STEM micrograph of  $Mo_4VC_4$  MXene showing a herringbone-type structure. An atomic schematic and mirror plane are shown by solid circles on the right and a dashed line, respectively. (G) SEM micrograph of a single  $Mo_4VC_4$  flake drop-cast onto a porous alumina substrate. (H) AFM micrograph of  $Mo_4VC_4$  flakes. (I) Height profiles of the AFM scans shown in H, showing an average thickness of 2.5 nm.

synthesis of  $Mo_4VAlC_4$  and the demonstration of  $Mo_4VC_4$  MXene shows that there is an additional family of phases to be explored with the potential for many other  $M_5X_4$  MXenes to be synthesized. Due to the increased number of atomic layers in their structure, MXenes with five atomic transition metal layers could potentially have exceptional mechanical properties allowing for stronger metal matrix composites, better EMI shielding capabilities,  $^{51}$  and higher electrical conductivity for electronic applications.

# **RESULTS AND DISCUSSION**

**Synthesis and Structural Characterization.** To identify the optimal chemistry for  $M_5AlC_4$  synthesis, we mixed six sets of starting powder mixtures with  $Mo_x:V_{5-x}$  ratios where x=5, 4, 3, 2, 1, and 0. We performed X-ray powder diffraction measurements on the powder produced after the MAX synthesis process at 1650 °C and determined that only the sample with a Mo:V ratio of 4:1 produced a  $M_5AlC_4$  phase, as shown in Supporting Figure 1. Then, a smaller interval was selected, where x=3.50, 3.75, 4.00, 4.25, and 4.50. These

studies indicate that the Mo:V ratio range for which a  $M_sAlC_4$  phase is stable is very narrow. These results are further discussed in Supporting Information (Supporting Figure 2). In brief, the  $Mo_xV_{5-x}AlC_4$  phase can be synthesized when the Mo:V ratio in the initial mixed powders is between 3.75:1.25 and 4.25:0.75. Supporting Figure 2 also shows an expansion in the a lattice parameter (a-LP) with increasing Mo content, which indicates that different Mo:V ratios are possible in the (MoV) $_5AlC_4$  structure, most likely as a solid-solution of Mo and V on the M sites. For the remainder of the characterization and synthesis of MXene described subsequently, we used (MoV) $_5AlC_4$  synthesized by mixing precursor powders with a Mo:V ratio of 4:1.

We also used XRD to examine the crystal structure of both the  $Mo_4VAlC_4$  MAX phase and  $Mo_4VC_4$  MXene (Figure 2).  $Mo_4VAlC_4$  has a structure similar to other MAX phases; however, several of the peaks in the XRD pattern do not exactly match with the characteristic peaks of a typical  $P6_3/mmc$  MAX structure. The (002) peak occurs at 6.26° indicating a c lattice parameter (c-LP) of 28.22 Å, which is

Table 1. EDS Measurements of Mo:V:Al:C:F:O Atomic Ratios for the MAX Phase (3 Particles Measured), Multilayer MXene (6 Particles Measured), and Free-Standing Film of Delaminated MXene (5 Spots Measured)<sup>a</sup>

sample	Mo	V	Al	С	F	О
$Mo_4VAlC_4$	$3.89 \pm 0.02$	$1.11 \pm 0.02$	$0.29 \pm 0.13$	$0.41 \pm 0.08$	-	$0.15 \pm 0.02$
Mo <sub>4</sub> VC <sub>4</sub> (multilayer)	$4.06 \pm 0.07$	$0.94 \pm 0.07$	-	$5.72 \pm 0.46$	$0.54 \pm 0.03$	$1.83 \pm 0.07$
Mo <sub>4</sub> VC <sub>4</sub> (delaminated)	$4.04 \pm 0.04$	$0.96 \pm 0.04$	-	$1.80 \pm 0.29$	$0.01 \pm 0.01$	$0.47 \pm 0.12$

"The values shown are atomic percentage normalized so that (MoV) = 5. Error is defined as 1 standard deviation.

similar to (TiNb)<sub>5</sub>AlC<sub>4</sub>, as reported previously.<sup>50</sup> This is among the largest c-LP of the known MAX phases. For comparison,  $Ti_2AlC$ ,  $Ti_3AlC_2$ , and  $Ta_4AlC_3$  have *c*-LPs of 13.610 Å, <sup>52</sup> 18.578 Å, <sup>53</sup> and 23.708 Å, <sup>54</sup> respectively. Mo<sub>4</sub>VAlC<sub>4</sub> powder contains impurity phases of Mo<sub>2</sub>C, VC, Al<sub>4</sub>C<sub>3</sub>, and Al<sub>2</sub>O<sub>3</sub>. The Al<sub>4</sub>C<sub>3</sub> is dissolved during the HClcleaning step (Supporting Figure 3). The presence of Al<sub>2</sub>O<sub>3</sub> is most likely due to the addition of V<sub>2</sub>O<sub>3</sub> in the starting powder. As we describe in Supporting Information, although we do not fully understand the role of 0.05 mol of vanadium oxide in this MAX formation, its presence is required to form a M5AC4 phase with the conditions reported here. It is possible that the oxygen acts as a catalyst for this reaction by partially substituting for carbon on the lattice forming oxicarbide, which might stabilize the structure. Additionally, the extra heat produced during the thermal reduction of V<sub>2</sub>O<sub>3</sub> by Al might push the sample into the (MoV)<sub>5</sub>AlC<sub>4</sub> region of this quaternary phase diagram. Without the addition of V<sub>2</sub>O<sub>3</sub>, the resulting powder was Mo<sub>2</sub>C and VC (Supporting Figure 4).

Similar to other Al-containing MAX phases, we attempted to selectively etch the Al layers with hydrofluoric acid (HF). During the first centrifugation wash cycle after the HF selective etching, the supernatant had a slight green tint (Supporting Figure 5). This is likely due to the dissolution of V from the MAX/MXene since any V-containing impurities remaining after the HCl treatment, such as V-based carbides, would not be dissolved by HF. The process of optimizing the synthesis method is described in Supporting Information (Supporting Figures 6–7). After selective etching and the removal of the Al layers from the MAX structure, the resulting multilayer MXene (002) peak shifts to a lower  $2\theta$ , which is due to the increased c-LP (36.0 Å) compared to the MAX precursor (28.2 Å). This is comparable to other reported increases in c-LP after etching.<sup>37,44</sup> After delamination of the resulting powder with tetramethylammonium hydroxide (TMAOH), a colloid with a concentration of ~0.25 mg/mL was obtained. By vacuum filtering the colloid, a free-standing film of Mo<sub>4</sub>VC<sub>4</sub> was made. The (002) peak of the resulting film is shifted to an even lower  $2\theta$  after delamination as a result of the further increase in c-LP (39.4 Å) due to the exfoliation of the MXene flakes and intercalation of tetramethylammonium cations used in the delamination process. This indicates an increase in c-LP of 3.4 Å. Similar increases in c-LP after complete delamination have also been reported for other MXenes, such as Ti<sub>3</sub>C<sub>2</sub> (4.48 Å). $^{47}$ 

**Microscopy.** Scanning electron microscopy of Mo<sub>4</sub>VAlC<sub>4</sub> (Figure 3A) shows the typical layered structure for MAX phase particles. To confirm the five-transition-metal-layered structure of Mo<sub>4</sub>VAlC<sub>4</sub>, transmission electron microscopy was used (Figure 3B,C). The alternating layered structure—with darker layers occurring every sixth layer—suggests that slabs of Mo<sub>4</sub>VC<sub>4</sub> are sandwiched between single Al layers (layers of carbon atoms are not visible). HR-STEM high-angle annular dark field (HAADF) imaging shows brighter atomic layers

(lighter weight Al layers) alternating with slabs of darker atoms (heavier Mo/V layers) (Supporting Figure 8A). A selected area electron diffraction (SAED) pattern of the [001] zone axis confirms a hexagonal crystal structure (Figure 3B inset).

After etching, the Al is removed and the particles become accordion-like (Figure 3D). HR-STEM (Figure 3E,F) shows the five atomic layers of Mo/V that are no longer sandwiched between layers of Al, confirming that conversion to Mo<sub>4</sub>VC<sub>4</sub> MXene was achieved. Upon further examination at higher resolution, it was discovered that the center Mo/V plane of atoms is a twinned plane, forming a herringbone-type structure (Figure 3F). This clarifies why the XRD patterns did not completely match the typical P6<sub>3</sub>/mmc structure of MAX phases. Further research is required to fully determine the atomic positions and space group of Mo<sub>4</sub>VAlC<sub>4</sub> MAX and Mo<sub>4</sub>VC<sub>4</sub> MXene.

After delamination, some of the  $Mo_4VC_4$  colloid was drop-cast onto porous alumina, and SEM shows an individual 2D flake (Figure 3G). TEM micrographs of a single  $Mo_4VC_4$  flake (Supporting Figure 8B,C) show a thickness of ~1.3 nm which is similar to the thickness of the  $Mo_4VC_4$  slabs in the MAX structure. Atomic force microscopy results (Figure 3H,I) show the  $Mo_4VC_4$  MXene flake has a thickness of 2.50  $\pm$  0.33 nm. Comparatively,  $Ti_3C_2$  (n=2, a MXene with three transition metal layers) has a thickness of 1.60 nm when measured with AFM. Reported AFM thickness values include the MXene flake as well as any absorbed water molecules or other adsorbed species. The cross-section of a film of  $Mo_4VC_4$  flakes showing layers of delaminated flakes stacked flat on top of each other is provided in Supporting Figure 8D.

**Compositional Characterization.** After determining the atomic structure, we turned our attention to the composition. As a qualitative tool, we used energy-dispersive X-ray spectroscopy and standard-less quantification<sup>56</sup> to study the compositions of the Mo<sub>4</sub>VAlC<sub>4</sub> MAX phase particles after HCl washing, Mo<sub>4</sub>VC<sub>4</sub> multilayer MXene particles, and the freestanding film of delaminated MXene (Table 1). Since the MAX powder likely contained binary carbide impurities that remained after HCl washing, EDS analysis was done on particles with a visible layered structure, similar to Figure 3A, and the measured compositions were averaged. Surprisingly, the atomic percentage of aluminum was much lower than the stoichiometric amount for the MAX phase. Upon further examination with TEM, it was discovered that in addition to five-layer slabs of Mo/V sandwiched between Al layers, thicker slabs of Mo/V layers are also present in some locations (Supporting Figure 9). There are occasionally slabs of up to 20 Mo/V layers observed. This can explain why there is a lower than expected Al ratio. Additionally, the reduction of V<sub>2</sub>O<sub>3</sub> by Al to form Al<sub>2</sub>O<sub>3</sub> could also contribute to this and a high concentration of Al vacancies may be present. The MXene showed no presence of aluminum and instead showed the presence of fluorine and oxygen terminations  $(T_x)$ . This

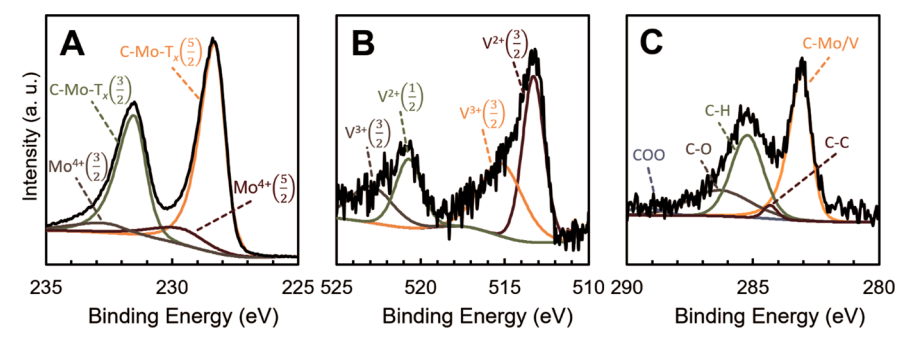


Figure 4. High-resolution XPS spectra of a Mo<sub>4</sub>VC<sub>4</sub> free-standing film. (A) Mo 3d. (B) V 2p. (C) C 1s regions.

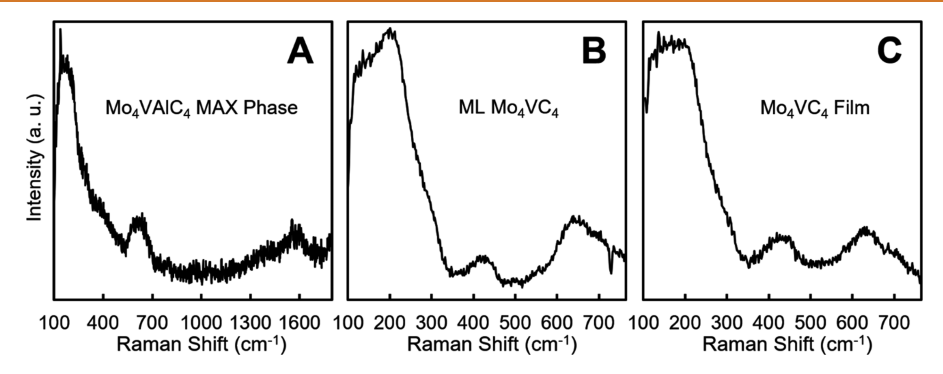


Figure 5. Raman spectra of MAX and MXene. (A) Mo<sub>4</sub>VAlC<sub>4</sub> MAX phase, (B) Mo<sub>4</sub>VC<sub>4</sub> multilayer MXene, and (C) free-standing film of delaminated Mo<sub>4</sub>VC<sub>4</sub> MXene.

indicates that the etching was successful, and terminations are present on the MXene surface.

While the Mo:V ratio used for synthesizing the Mo<sub>4</sub>VAlC<sub>4</sub> MAX phase was 4:1, the resulting material had a ratio of  $Mo_{3.89}:V_{1.11}$  (Table 1). After the HF treatment, the resulting Mo<sub>4</sub>VC<sub>4</sub> MXene had a ratio of Mo<sub>4.06</sub>:V<sub>0.94</sub>. After delamination with TMAOH, the ratio remained about the same-Mo<sub>4.04</sub>:V<sub>0.96</sub>. The fluctuations in the Mo:V ratio are likely within reasonable error of the EDS detector, which means the selective etching was done for Al layers. The slight change in the Mo/V ratio might also be due to dissolution of some V atoms from the surface layer of the carbide, which agrees with the green color of the solution during the first wash. The amount of F present decreases after delamination. It has been shown previously that delamination with TMAOH decreases the F content,<sup>57</sup> specifically for Mo-containing MXenes.<sup>58,59</sup> Nonetheless, the F content even before delamination is still significantly lower compared to Ti-based MXenes, 60 which is in agreement with previously reported work indicating that Mo on the surface preferentially bonds with -OH or =O terminations rather than -F. 61 Also, a decreased O content was observed after delamination; however, the accuracy of the EDS detector for O is limited so we do not report this as a quantitative result.

A high-resolution EDS spectrum was also obtained to determine whether the Mo/V layers were ordered or disordered solid-solutions (Supporting Figure 10). There is a distinct ordering with regard to the Mo/V slabs alternating with Al layers as shown by the periodic Al peaks. The spectra for Mo and V within the slabs are generally homogeneous, and therefore it is concluded that the Mo/V layers are solid-solutions of Mo and V. Despite this conclusion, a higher brightness of the middle layer (Supporting Figure 11) was

observed in select instances, suggesting possible enrichment with Mo.

X-ray photoelectron spectroscopy was used to quantify the transition metal ratio, and the C content in Mo<sub>4</sub>VC<sub>4</sub> MXene. The Mo 3d region (Figure 4A) can be adequately fitted with two doublets corresponding to Mo bonded to carbon and surface termination at 228.47 eV (231.68 eV) and Mo in the Mo<sup>4+</sup> oxidation state at 229.59 eV (232.83 eV), which corresponds to small amount of oxides presented in the freestanding film. Similarly, the V 2p region can also be fitted with two doublets centered at 513.38 eV (520.84 eV) and 514.94 eV (522.81 eV) corresponding to  $V^{2+}$  and  $V^{3+}$  states, respectively, as shown in Figure 4B.<sup>30</sup> Both doublets in the V 2p regions are assigned to V bonded to C atoms in the MXene structure. The difference in oxidation states of V might come from different surface terminations bonded on the V atom on the surface, which implies that V is positioned in different transition metal layers (bonded to C and terminations), another indication of solid-solution in the transition metal layers. The C 1s region (Figure 4C) was fitted by 5 peaks, corresponding to C-Mo/V, C-C, C-H, C-O, and C-OO at 283.15, 284.56, 285.31, 286.48, and 289.12 eV, respectively. The atomic ratio was deduced from the intensity of only the peaks related to MXene, e.g., only C-Mo/V peak in C region was used in this calculation. The calculated ratio was Mo<sub>4,10</sub>V<sub>0,90</sub>C<sub>2,99</sub> which agrees with the ratio of Mo:V obtained from EDS results. The amount of C is below the expected stoichiometry, similar to many MXenes, possibly because of the presence of C vacancies in their precursor MAX phases. 62 This high concentration of C vacancies may also be required to form this higher n MAX phase. It was shown for V<sub>4</sub>AlC<sub>3</sub> that the structure is only stable with the presence of 11% carbon vacancies. 63 The low amount of C could also be due to a substitution of O for some of the C sites during the

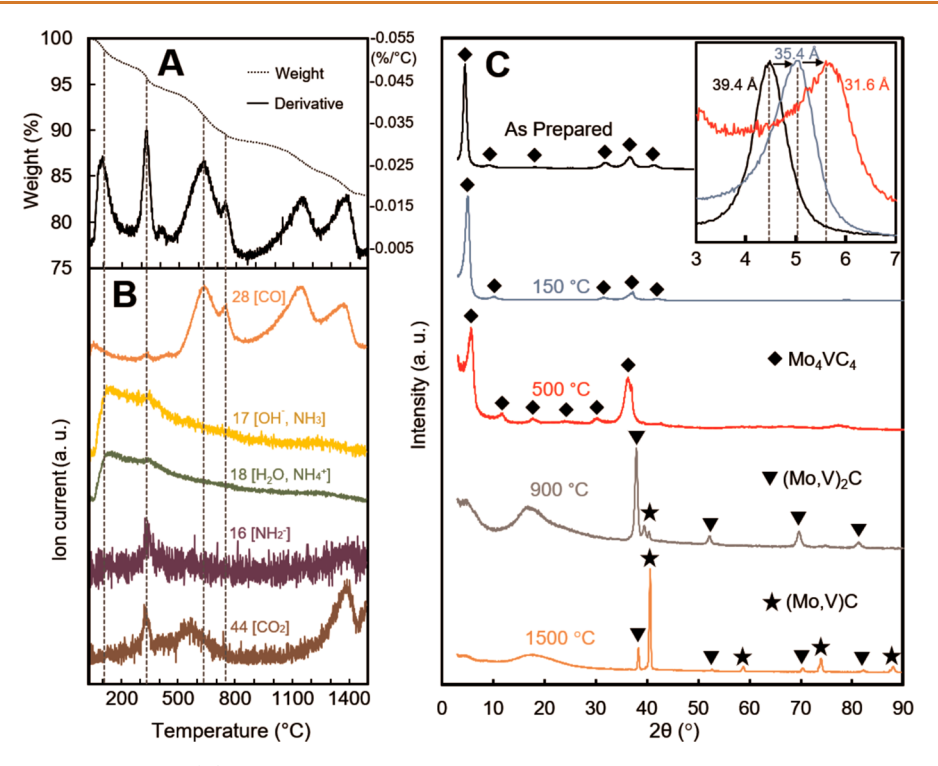


Figure 6. Thermal stability of  $Mo_4VC_4$ . (A) Thermogravimetric analysis of  $Mo_4VC_4$  MXene film. The sample experienced 6 drops in its weight due to water,  $OH^-$  termination groups, TMAOH, and the MXene decomposition. (B) Mass spectrometry results indicating the removal of CO,  $OH^-/NH_3$ ,  $H_2O/NH_4^+$ ,  $NH_2^-$ , and CO<sub>2</sub> from the MXene film that correspond to the sample's weight loss. (C) XRD patterns of the resulting material after the drops in sample weight. Inset shows a close view of the peak shift in the XRD pattern of the material as prepared, heated to 150 °C, 500 °C, and 900 °C with the respective c-LPs. The broad peaks at ~20° in the 900 and 1500 °C patterns are due to the double-sided tape that was used to hold the film pieces to the glass slide during XRD measurements.

synthesis of Mo<sub>4</sub>VAlC<sub>4</sub> MAX phase. XPS results also indicate that no Al is present after etching and the amount of F surface termination is very small, in agreement with our EDS results (no more than 10% of the total surface termination) (Supporting Figure 12 A,B).

The Raman spectra of HCl-washed Mo<sub>4</sub>VAlC<sub>4</sub>, multilayer Mo<sub>4</sub>VC<sub>4</sub>, and a free-standing film of delaminated Mo<sub>4</sub>VC<sub>4</sub> MXene (Figure 5) show broad peaks in the range below 1000 cm<sup>-1</sup> that correspond to vibrations of metals with oxygen and carbon. Both molybdenum and vanadium carbides exhibit bands below 700 cm<sup>-1</sup>. Cubic VC exhibits one band<sup>64</sup> at 250 cm<sup>-1</sup>, and hexagonal Mo<sub>2</sub>C shows a number of peaks around 143 cm<sup>-1</sup> as well as one band at 650 cm<sup>-1</sup>.<sup>65</sup> Aluminum carbide has a distinct band around 850 cm<sup>-1</sup>.<sup>66</sup> The band position is at higher frequencies due to atomic mass differences between Mo, V, and Al. No bands around 850 cm<sup>-1</sup> are found in the Raman spectrum of MAX phase which suggests the absence of Al<sub>4</sub>C<sub>3</sub> in the MAX phase.

Raman spectra have been described for MXenes with other *n* values such as M<sub>2</sub>X<sub>5</sub><sup>67</sup> M<sub>3</sub>X<sub>2</sub><sup>68</sup> and M<sub>4</sub>X<sub>3</sub>.<sup>69</sup> Following the trend, Mo<sub>4</sub>VC<sub>4</sub> is expected to exhibit M, X, and T<sub>x</sub> group vibrations, T<sub>x</sub> atom vibrations, and X atom vibrations. The obtained spectra follow this trend. Three regions of vibrations are observed. The region between 100 and 300 cm<sup>-1</sup> corresponds to V, Mo, C, and surface group vibrations followed by the surface group region at 350–500 cm<sup>-1</sup> and carbon vibration region at 500–700 cm<sup>-1</sup>. The peaks are broad and overlapping. In contrast, Raman spectra of ordered MXenes Mo<sub>2</sub>TiC<sub>2</sub> and Mo<sub>2</sub>Ti<sub>2</sub>C<sub>3</sub> exhibit sharp bands in the region below 1000 cm<sup>-1</sup>.<sup>27</sup> Since Raman vibrations in solids represent the vibrations of a unit cell, distortions of

neighboring unit cells due to varying M-elements will lead to broadening of Raman peaks due to different frequencies of the vibrations. Moreover, since Raman bands depend on the element's mass, broadening will be even more pronounced when the interchangeable elements have a large difference in mass. This again indicates that there are solid-solutions on the M sites within the MAX and MXene structure. Additionally, traces of free carbon are observed in the MAX phase sample (the peak at about 1600 cm<sup>-1</sup>).

**Thermal Analysis.** The thermal stability of a Mo<sub>4</sub>VC<sub>4</sub> film was determined by thermogravimetric analysis coupled with mass spectrometry (MS) under Ar flow. The thermogram (Figure 6A) shows several significant drops in the weight of the sample upon heating. The first weight loss step, which peaked at 125 °C, is due to the removal of H<sub>2</sub>O molecules that were trapped in between the Mo<sub>4</sub>VC<sub>4</sub> flakes from the filtration of the MXene colloid as shown by the H<sub>2</sub>O and OH<sup>-</sup> peaks in the mass spectra (Figure 6B).26 The XRD pattern of a sample treated at 150 °C under Ar flow (Figure 6C) reveals a shift in the (002) peak indicating a decrease in c-LP of 4 Å from the as-prepared sample. This is due to the compaction of the flakes after the H<sub>2</sub>O removal. The amount of compaction indicates that possibly two layers of H<sub>2</sub>O molecules were present as the molecular radius of  $H_2O$  is  $\sim 2.75$  Å. The second weight loss step, which peaked at 342 °C, is due to the removal of residual TMAOH between the flakes as shown by the NH<sub>2</sub>-, CO<sub>2</sub>, CO, OH<sup>-</sup>/NH<sub>3</sub>, and H<sub>2</sub>O/NH<sub>4</sub><sup>+</sup> peaks in the mass spectra (Figure 6B). 25,26,71 For a sample treated at 500 °C under Ar flow, there is a further shift in the (002) peak indicating a decrease in c-LP of 3.8 Å from the sample treated at 150 °C and a total of 7.8 Å decrease in c-LP from the as-prepared sample (Figure 6C).

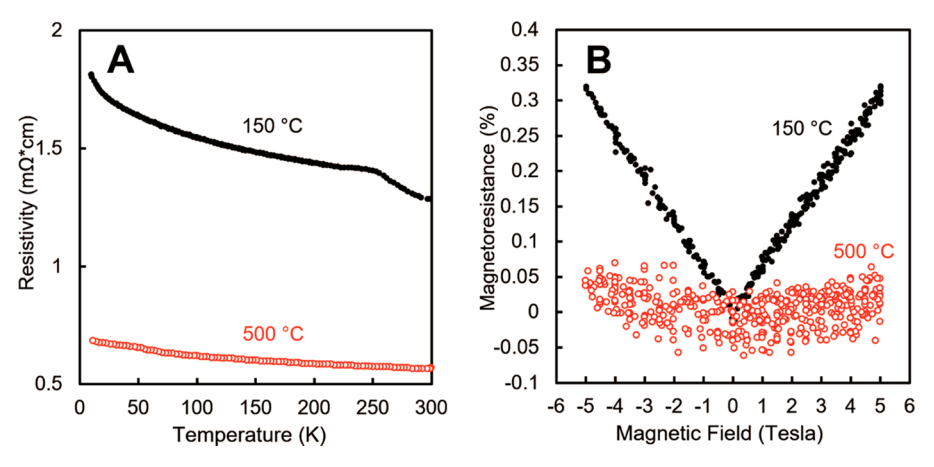


Figure 7. Temperature-dependent electrical properties of MXene. (A) Electrical resistivity as a function of temperature for  $Mo_4VC_4$  annealed at 150 and 500 °C. (B) Magnetoresistance of  $Mo_4VC_4$  under an external magnetic field perpendicular to the sample surface.

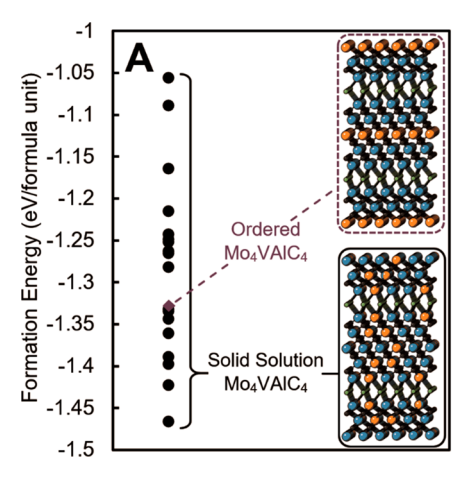
This decrease in c-LP from as-prepared to treated at 500 °C is smaller than those reported for  $Mo_2C$  (17.9 Å),  $Mo_2TiC_2$  (13.3 Å), and  $Mo_2Ti_2C_3$  (15 Å), possibly because those MXenes were delaminated with tetrabutylammonium hydroxide which has a larger radius of 8–9.9 Å.<sup>27</sup> The removal of additional water suggests that some is retained even after the weight loss step at 125 °C. The ionic radius of  $TMA^+$  is 3.2 Å, which indicates that there is likely one layer of  $TMA^+$  ions between the layers with some  $H_2O$  retained.

Overall, our TGA-MS results show that H<sub>2</sub>O and TMA<sup>+</sup> ions occupy similar amounts of space between the MXene flakes. The temperatures for the removal of residual H<sub>2</sub>O and TMAOH are in agreement with previously reported results for another Mo-containing MXene; Mo<sub>2</sub>C.<sup>26</sup> Our results indicate that Mo-containing MXenes have similar thermal behaviors due to similar bonding strengths between Mo and molecules on the surface, but these behaviors have been shown to be different than MXenes with other M elements. The next weight loss began at ~505 °C and was indicated by C leaving the structure as CO. This is similar to the behavior exhibited by Mo<sub>2</sub>C.<sup>26</sup> Defunctionalization of the surface producing two peaks at 638 and 742 °C (Figure 6A) allows recrystallization of carbide. After the heat treatment at 900 °C under Ar flow the resulting material is no longer Mo<sub>4</sub>VC<sub>4</sub> MXene, and instead decomposes to form an orthorhombic (Mo,V)2C phase. Heating to 1500 °C transformed much of the orthorhombic (Mo,V)<sub>2</sub>C phase to cubic (Mo,V)C, as marked in Figure 6C. However, the exact structure of these bulk carbides was not analyzed in this study.

Electrical and Optical Properties. The electrical resistivity of an as-prepared Mo<sub>4</sub>VC<sub>4</sub> free-standing film was measured with a 4-point probe. The thickness and resistivity values were quite uniform (standard deviation = 0.82  $\mu$ m and  $0.10 \text{ m}\Omega$  cm, respectively). The resistivity was measured to be 4.18 m $\Omega$  cm (conductivity 240 S/cm). To remove the effects of water and TMAOH intercalants, the as-prepared sample was heated at 500 °C in an Ar atmosphere for 5 h. We chose 500 °C annealing temperature based on our TGA results (Figure 6). After heat-treatment, the sample's electrical resistivity decreased to 1.20 m $\Omega$  cm (conductivity 833 S/cm). This electrical resistivity is similar to another Mo-based MXene;  $Mo_2Ti_2C_3$  (1.63 m $\Omega$  cm).<sup>27</sup> Interestingly, two thinner Mobased MXenes, Mo<sub>2</sub>C and Mo<sub>2</sub>TiC<sub>2</sub>, have much lower resistivities of 0.80 m $\Omega$  cm and 0.67 m $\Omega$  cm, respectively. It is expected that a thicker MXene would have a lower resistivity due to additional paths for electrons to travel within a flake; however, this is not the case for the film measured here. We hypothesize that due to the increased thickness of  $\mathrm{Mo_4VC_4}$ , the flakes are probably more rigid and might not stack well and might have gaps between adjacent flakes leading to fewer conductive paths. In other words, this can be due to the interflake resistivity rather than the intraflake resistivity. New measurement techniques are needed to measure the intrinsic properties of MXenes, such as electrical resistivity.

The electrical resistivity of Mo<sub>4</sub>VC<sub>4</sub> films as a function of temperature was measured after drying at 150 °C in a vacuum oven and annealing at 500 °C under an Ar atmosphere. The results (Figure 7A) show that the resistivity gradually increases as temperature decreases. The trend was similar for both samples, although the sample annealed at 500 °C had a slightly lower absolute resistivity. Interestingly, the room-temperature resistivity of this MXene only reduced by  $\sim 0.4$  m $\Omega$  cm, compared to the dried sample, after annealing at 500 °C. This indicates that large *d*-spacing caused by TMAOH intercalation does not largely affect the electron transport property of this MXene, unlike what was observed for Ti<sub>3</sub>CN MXene, where an order of magnitude reduction in room-temperature resistivity was observed after annealing at 400 °C. 25 The smaller decrease in resistivity could also be due to poor stacking of thick and rigid Mo<sub>4</sub>VC<sub>4</sub> flakes, so that even after annealing, the flakes do not align well, having poor connections with neighboring flakes, as discussed above. The effect of TMAOH on temperature-dependent resistivity can be seen by comparing the overlaid temperature-dependent resistivity curves for as produced and annealed MXene (Supporting Figure 13A). The trend is similar although the 500 °C-annealed sample exhibits a less drastic increase in resistivity with decreasing temperature. The abrupt increase of the resistivity seen in the 150 °Cannealed sample (black curve) at ~250 K is most likely due to freezing of the remaining water and TMAOH molecules.

The magnetoresistance was measured at 10 K with a magnetic field up to 5 T applied perpendicular to the sample surface. Mo<sub>4</sub>VC<sub>4</sub> exhibits a positive MR as shown in Figure 7B, which is similar to other Mo-containing MXenes, <sup>58,59</sup> while many other MXenes exhibit a negative MR. <sup>58,72</sup> The reason for the positive MR observed in Mo-containing MXenes is currently unclear and a topic requiring further research. However, the strength of magnetoresistance was almost negligible for the sample annealed at 500 °C. This indicates that the magnetoresistance might be related to interflake



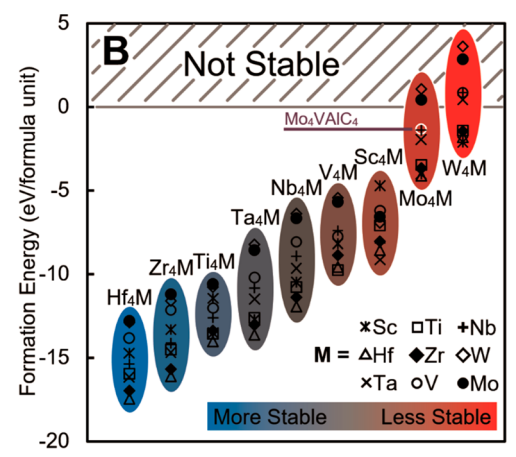


Figure 8. DFT predictions of MAX phases and MXenes. (A) Formation energies for solid-solution Mo<sub>4</sub>VAlC<sub>4</sub> configurations (black dots) compared to ordered Mo<sub>4</sub>VAlC<sub>4</sub> (purple diamond). (B) DFT calculated formation energies of ordered M'<sub>4</sub>M"AlC<sub>4</sub> MAX phases. Most are predicted to be stable except for some Mo and W compositions.

electron transport rather than an intrinsic property of the MXene flakes. Hall measurements of both samples at 10 K indicates carrier concentration of  $2.52 \times 10^{22}$  cm<sup>-3</sup> and  $1.37 \times 10^{22}$  cm<sup>-3</sup> for the 150 °C- and 500 °C-annealed samples, respectively. Both samples exhibit negative Hall slope (Supporting Figure 13B) suggesting that electrons are the major carrier. The carrier mobility increases from 0.10 cm<sup>2</sup>/V s for the 150 °C-annealed samples to 0.36 cm<sup>2</sup>/V s for the 500 °C-annealed samples, mostly likely due to less scattering in the absence of TMAOH and water.

The optical properties were evaluated by measuring the extinction per path length (Ext/l) of delaminated Mo<sub>4</sub>VC<sub>4</sub> solutions with varying concentrations and transmission of Mo<sub>4</sub>VC<sub>4</sub> thin films (Supporting Figures 14-15). As determined with UV-vis-NIR spectroscopy, the extinction coefficient at 550 nm ( $\varepsilon_{550}$ ) was determined to be 34.4 L g<sup>-1</sup> cm<sup>-1</sup>. Thin film transmission measurements show there is a decrease in transparency with increasing wavelength from 300 to 1000 nm (Supporting Figure 15). MXenes with an n value of 1 or 2, such as Ti<sub>2</sub>C, V<sub>2</sub>C, Ti<sub>3</sub>CN, and Ti<sub>3</sub>C<sub>2</sub>, interact with light within the visible spectrum displaying composition-dependent extinction.  $^{13,14,74}$  Notably,  $\mathrm{Ti_2C}$  shows a broad extinction peak at 550 nm, which shifts to lower energy for Ti<sub>3</sub>C<sub>2</sub>, as indicated by a broad extinction peak between 700 and 800 nm and strong decrease in transparency in the infrared region.<sup>14</sup> In comparison, Mo<sub>4</sub>VC<sub>4</sub> exhibits a featureless absorption spectrum from the visible to near-infrared range (400 to 2500 nm), hinting at fundamental differences in how the material interacts with electromagnetic radiation compared to MXenes with a n value of 1 or 2. To the best of our knowledge, the optical properties of MXenes with n larger than 2 have not been reported and future studies exploring the relationship between atomic thickness and optical properties are imperative. Due to the featureless spectrum, a potential application of this material could include fabricating low loss and high optical figure of merit (FOM) transparent conducting electrodes. Realization of this application will require efforts focused on optimization of the thin film quality and identification of the optical coefficients in the wavelength region in which the material will operate.

**Density Funtional Theory.** Density functional theory calculations were performed to determine the preferred termination groups that can exist on the surface of Mo<sub>4</sub>VC<sub>4</sub>

MXene. The results of these calculations indicate that -OH is the most preferred termination group with -9.10 eV formation energy. =O and -F terminations are not as stable (-5.39 eV and -6.56 eV, respectively) which agrees with the experimental results presented here (Figure 4). With regard to the Mo<sub>4</sub>VAlC<sub>4</sub> MAX phase, DFT calculations were used to determine the stabilities of 18 quasirandom solid-solution configurations as well as an ordered configuration with one layer of V sandwiched between four layers of Mo (two layers of Mo on each side as shown in Figure 8A). Examples of these quasi-random structures are provided in Supporting Figure 16. Each of these phases were predicted to be stable, in agreement with experimental results. For Mo<sub>4</sub>VAlC<sub>4</sub>, there are solidsolution configurations that are more stable than an ordered configuration; thus, it is more preferred for Mo<sub>4</sub>VAlC<sub>4</sub> to exist as a solid-solution. The most stable solid-solution configuration that we calculated had a and c lattice parameters of 3.04 and 28.52 Å, respectively. This agrees well with our experimental results obtained with XRD (a = 2.99 and c =28.22 Å).

DFT calculations were also performed to determine the thermodynamic stability of other  $M_5AlC_4$  MAX phases. Specifically, the formation energies of ordered  $M'_4M''AlC_4$  compositions were calculated where M' and M'' were Hf, Zr, Ti, Ta, Nb, V, Sc, Mo, and W. A summary of the predicted stability of these phases is shown in Figure 8B. The exact formation energy values are provided in Supporting Table 2. It is expected for many of the compositions examined here, that there may be at least one solid-solution structure that is more stable than the compositionally equivalent ordered structure. We present calculations for ordered MAX structures as a simple exploration of stability trends and many of their compositionally equivalent  $M'_4M''AlC_4$  solid-solution phases will likely be even more stable.

Interestingly, other phases studied, such as ordered phases containing Hf, Zr, and Ta, are predicted to be more stable than the synthesized  $Mo_4VAlC_4$ . The effect that the M' element has on the stability was determined to be much greater than that of M''. W- and Mo-containing compositions are the least stable and are the only two M' elements that produce some unstable compositions. For both Mo- and W-based MAX phases specifically, it is known that Mo and W avoid stacking with C in a face-centered cubic structure (FCC),  $^{40}$  so adding another

M element can allow for Mo- and W-based MAX/MXene to be synthesized as the additional M element will occupy some of the FCC sites, thus relieving stress within the crystal structure. However, here we considered only ordered phases in Figure 8B and compositions predicted to be unstable may still have other stable solid-solution configurations. These calculations also show that most of the M elements can achieve a higher stability when they are combined with another M element. The only exception to this is Hf which is most stable when M' = M''. Worth noting are the specific elements that best stabilize the material. Higher stability occurs when Hf, Zr, Ti, and Ta are the M' or M" element. This agrees with previous work where these elements were predicted to stabilize MAX phases,<sup>63</sup> and the lower formation energies were correlated with the difference in ionic radius between the M atoms.<sup>75</sup> MAX phases with M = Cr or Mn are reserved for a future study, as we expect many of these phases have stable magnetic ground states, and a more detailed study is needed to properly characterize these systems.

To thoroughly explore the configurational space of the  $Mo_4VAlC_4$  system, we performed cluster expansion calculations around the concentration  $X_{Mo}=0.8$  with the ATAT (Alloy Theoretical Automated Toolkit) package (Supporting Table 3). The converged ground-state solid-solution structure has an energy 15.8 meV/atom lower than the ordered symmetric phase. The low energy structures generated during the cluster expansion calculations show that V avoids the middle layer in solid-solution. In this composition range, V prefers to occupy layers 2 and 4 in order to maximize the number of favorable Mo–V bonds and stabilize the crystal structure.

Based on the crystal structure observed with TEM, we have additionally examined a nontypical MAX phase structure— Mo<sub>4</sub>VAlC<sub>4</sub> with P6m2 symmetry, rather than the traditional P6<sub>3</sub>/mmc space group,<sup>77</sup> because this symmetry exhibits a herringbone-type structure like that observed with TEM, and the simulated XRD pattern for this structure matches well with our experimental results. We find that the Mo<sub>4</sub>VAlC<sub>4</sub> phase exhibiting P6m2 symmetry also prefers a disordered solidsolution, with a solid-solution ground-state energy that is 67.8 meV/atom lower than the ordered, symmetric phase. The low energy structures exhibit the same Mo-rich middle layers. Interestingly, the ground state in the  $P\overline{6}m2$  geometry is 31.8 meV/atom lower in energy than the ground state in the P6<sub>3</sub>/ mmc geometry. This indicates that further study, both experimentally and theoretically, is required to confirm the structure of Mo<sub>4</sub>VAlC<sub>4</sub> and other theoretically predicted quaternary M<sub>5</sub>AlC<sub>4</sub> phases. However, the disordered nature and Mo-rich inner layer are independent of the space group.

These calculations show that there is potential for expansion to other  $M_5AlC_4$  MAX phases, allowing for more  $M_5X_4$  MXenes to be produced. It is important to note that while many of these ordered  $M'_4M''AlC_4$  phases were determined to be stable compared to their respective unary phases, there may be binary carbides, intermetallics, or other competing MAX phases that are more stable for these compositions. Full evaluation of the possibilities for the synthesis of more  $M'_4M''X_4$  MXenes requires solid-solution calculations, precise determination of this five-layered crystal structure, dynamical and phase stability analysis, and calculation of exfoliation energies. The work presented here provides only trends in stability as a function of M element composition. Future studies will include detailed examinations of solid-solutions

over various compositions and stability with respect to other competing phases. The results presented here give some insight and direction into the huge space of additional structures to explore with computation and machine learning<sup>78</sup> to accelerate the expansion of the MXene family.

#### **CONCLUSIONS**

Here, we report Mo<sub>4</sub>VC<sub>4</sub>, a MXene with nine atomic layers (five transition metal and four carbon) synthesized from a M<sub>5</sub>AX<sub>4</sub> phase precursor, Mo<sub>4</sub>VAlC<sub>4</sub>, that contained no other MAX phase impurities. Mo<sub>4</sub>VAlC<sub>4</sub> is the only known MAX phase to exhibit twinning on the center M layers of atoms, which makes Mo<sub>4</sub>VC<sub>4</sub> MXene different from all other known MXenes for the two reasons stated above. This MXene is disordered on the M site as indicated by high-resolution EDS. Besides the scalable synthesis method, we present structural and chemical analysis of both Mo<sub>4</sub>VAlC<sub>4</sub> and Mo<sub>4</sub>VC<sub>4</sub>, as well as thermal stability, optical, and electronic characterization of Mo<sub>4</sub>VC<sub>4</sub>. In addition, DFT results show the great potential for discovering additional M5AX4 phases. Due to their higher thickness, M<sub>5</sub>X<sub>4</sub> MXenes could have the potential to be useful in many applications including, but not limited to, structural materials, optoelectronic devices with high figure of merit, and electronics. Mo<sub>4</sub>VAlC<sub>4</sub> MAX phase and Mo<sub>4</sub>VC<sub>4</sub> MXene venture into the M<sub>5</sub>X<sub>4</sub> territory for the MXene family of 2D materials.

### **EXPERIMENTAL METHODS**

Synthesis of Mo<sub>4</sub>VAlC<sub>4</sub> MAX. Molybdenum (99.9% Alfa Aesar, -250 mesh), vanadium (99.5% Alfa Aesar, -325 mesh), vanadium-(III) oxide (98% Sigma-Aldrich), aluminum (99.5% Alfa Aesar, -325 mesh), and graphite (99% Alfa Aesar, -325 mesh) powders were hand-mixed with an agate mortar and pestle for 5 min in a molar ratio of 4:0.9:0.05:1.2:3.5 (Mo:V:V<sub>2</sub>O<sub>3</sub>:Al:C). To determine the proper Mo:V mixing ratio, we mixed a series different ratios from 0% to 100% Mo (Supporting Figure 1). The mixtures were heated in alumina crucibles at a rate of 3 °C/min to 1650 °C under 350 cm<sup>3</sup>/min flowing argon in a tube furnace (Carbolite Gero) and held for 4 h before passive cooling to room temperature. After removal from the furnace, the sintered blocks of Mo<sub>4</sub>VAlC<sub>4</sub> MAX phase were drilled with a tabletop drill press with a carbide drill bit to form a powder. To dissolve metallic and oxide impurities, 15 g of this powder was then stirred in 50 mL of HCl (36.5-38% Fisher Chemical) for 18 h. The HCl was washed out through a series of centrifugations at 3500 rpm (2550 rcf) for 3 min, decanting the acidic supernatant, and redispersing the sediment in deionized (DI) water. The exact washing procedure is described in Supporting Information. After washing, the MAX powder was dried in a vacuum desiccator for 18 h at 25 °C. Then the powder was sieved to a particle size  $<75 \mu m$ .

**Synthesis of Mo<sub>4</sub>VC<sub>4</sub> MXene.** A simplified schematic for the synthesis of Mo<sub>4</sub>VC<sub>4</sub> MXene is shown in Figure 9. To synthesize multilayer MXene, 4 g of the MAX powder was slowly added to 40 mL of HF (48–51% Arcos Organics). The sample was stirred with a polytetrafluoroethylene (PTFE)-coated stir bar at 400 rpm and heated in an oil bath at 50 °C for 8 days. After that, the mixture was washed with the same washing procedure previously described in the MAX synthesis section (detailed washing procedure is described in Supporting Information). After the pH of the mixture was more than 6, the multilayer MXene was collected on a MF-Millipore 0.45  $\mu$ m mixed cellulose esters (MCE) membrane by vacuum-assisted filtration. The wet multilayer MXene powder was then dried in a vacuum desiccator for 18 h at 25 °C.

Exfoliation of the multilayer MXene was achieved by dispersing 0.25 g of multilayer  $Mo_4VC_4$  powder in a 10 mL solution of 10 wt % tetramethylammonium hydroxide (TMAOH, 25 wt % – diluted to 10 wt %, Sigma-Aldrich) and stirred at 400 rpm at 25 °C for 24 h.

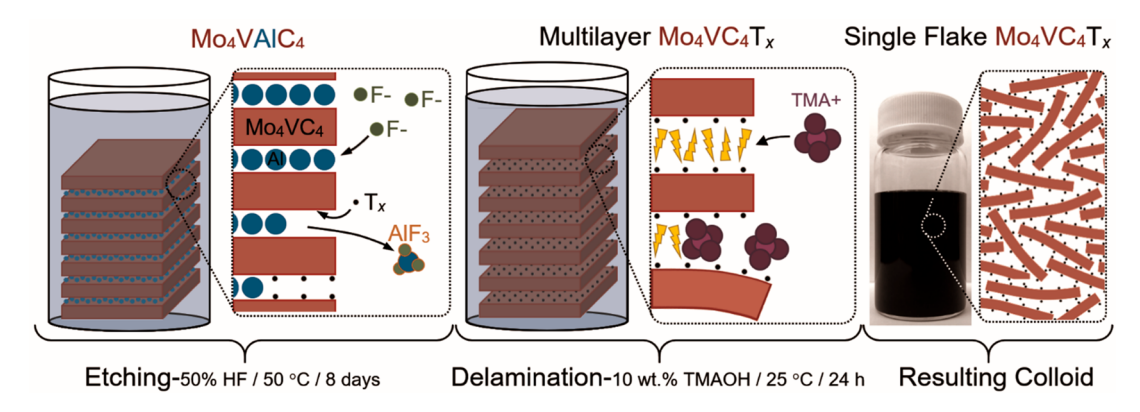


Figure 9.  $Mo_4VAlC_4$  MAX phase is etched with HF to produce  $Mo_4VC_4$  MXene. The fluorine ions selectively remove the Al layers of the MAX structure to form  $AlF_3$  and surface terminations bond to the basal planes of the resulting MXene. Afterward, the MXene flakes are held together by weak van der Waals forces and can be delaminated by introducing tetramethylammonium (TMA<sup>+</sup>) ions that intercalate between the layers, forcing them apart. This results in a colloidal suspension of 2D MXene flakes.

Another series of washing cycles was used to remove the TMAOH, as detailed in Supporting Information. In brief, the mixture was centrifuged at 8000 rpm (8230 rcf) for 30 min to settle the material and, after decanting the alkaline supernatant, the sediment was redispersed with DI water and this was repeated 5 times. High-speed centrifugation was needed due to the stability of the Mo<sub>4</sub>VC<sub>4</sub> flakes in the alkaline solution. Once the decanted supernatant had a pH < 8, the remaining sediment was redispersed in 30 mL of DI water and bath sonicated (100 W, 40 kHz) for 1 h with argon bubbling through it. After sonication, the solution was centrifuged at 3500 rpm (2550 rcf) for 1 h. The resulting supernatant was carefully removed with a pipet to avoid redispersal of, and contamination with, the multilayer MXene/MAX phase sediment and transferred into a separate bottle.

Mo<sub>4</sub>VC<sub>4</sub> Film Preparation. To obtain a free-standing film of Mo<sub>4</sub>VC<sub>4</sub>, the colloid containing delaminated MXene flakes was filtered by vacuum-assisted filtration through a Celgard membrane (Celgard 3501–64 nm porous polypropylene). The resulting MXene films were dried in a vacuum desiccator for 18 h at 25 °C.

**Structural Characterization.** Crystal structures were characterized with XRD. Rigaku SmartLab and MiniFlex X-ray diffractometers were used and Ni-filtered Cu–K $\alpha$  radiation was used at 40 kV/30 mA and 40 kV/15 mA, respectively. The step size of the scan was 0.01° with a step duration of 4 s for the as-produced Mo<sub>4</sub>VAlC<sub>4</sub> and 2 s for the multilayer Mo<sub>4</sub>VC<sub>4</sub> powder and Mo<sub>4</sub>VC<sub>4</sub> film. Supporting Table 1 provides the position of XRD peaks, d spacings, and corresponding intensities for the as-prepared Mo<sub>4</sub>VAlC<sub>4</sub> sample powder from 3° to 120°.

**Microscopy.** SEM micrographs were obtained with a Zeiss Supra 50VP scanning electron microscope and an FEI Strata DB235 Dual Beam Focused Ion Beam SEM. Transmission electron microscopy (TEM), scanning transmission electron microscopy (STEM), and selected area electron diffraction (SAED) were performed on a JEOL JEM F200 and JEOL NEOARM at an operating voltage of 200 kV. The colloid containing delaminated Mo<sub>4</sub>VC<sub>4</sub> flakes and particles of Mo<sub>4</sub>ValC<sub>4</sub> and multilayer Mo<sub>4</sub>VC<sub>4</sub> were drop-cast onto TEM grids. AFM was performed with a Bruker Multimode 8 with a Si tip (Budget Sensors Tap300Al-G;  $f_0 = 300 \text{ kHz}$ , k = 40 N/m) with a standard tapping mode in air. The colloid containing delaminated Mo<sub>4</sub>VC<sub>4</sub> flakes was drop-cast onto oxygen plasma-cleaned SiO<sub>2</sub>/Si wafers for the AFM measurement.

Compositional Characterization. Chemical compositions were determined by EDS measurements. EDS spectra of the MAX phase and multilayer MXene particles, drop-cast onto carbon tape, were recorded by a FEI Strata DB235 Dual Beam Focused Ion Beam SEM with EDS with a 25 kV beam and an average of 360,000 counts per spectrum. High-resolution EDS spectra of the MAX and MXene atomic layers were recorded with a JEOL NEOARM operating in STEM mode at 200 kV.

Chemical compositions were also determined with XPS. XPS spectra were collected by a spectrometer (Physical Electronics, Versa Probe 5000, MN) using a monochromatic Al K $\alpha$  X-ray source with 200  $\mu$ m spot size. Charge neutralization was performed using a dual-beam charge neutralizer. The sample was sputtered with Ar ions (2 kV, 2  $\mu$ A) for 2 min inside the analysis chamber. High-resolution spectra were collected at a pass energy of 23.5 eV with a step size of 0.05 eV, whereas the survey spectra were collected at a pass energy of 117 eV with a step size of 0.5 eV. The quantification and peak fitting of the core-level spectra was performed using Casa XPS software package with Shirley-type background.

Raman spectra were obtained with an inverted reflection mode Renishaw (2008, Gloucestershire, UK) instrument, equipped with  $63\times$  (NA = 0.7) objectives and a diffraction-based room-temperature spectrometer. The laser line used was 514 nm (Ar laser with 488 and 514 nm emissions) with an 1800 line/mm grating. The power of the laser was kept in the ~0.5–1 mW range. Mapping was performed by raster scanning in the streamline mode at a 0.5  $\mu$  x-axis step, the final spectra were an average of all collected data. Fitting was performed in Renishaw WiRE 3.4 software. The Mo<sub>4</sub>VAlC<sub>4</sub> MAX phase and Mo<sub>4</sub>VC<sub>4</sub> multilayer MXene powder were pressed in a 13-mm-diameter die to form pellets that were analyzed with the spectrometer.

Optical Properties. UV-vis-NIR spectrophotometry spectra were obtained by spray-coating thin films of Mo<sub>4</sub>VC<sub>4</sub> onto oxygen plasma-cleaned glass slides. Films of various thickness were measured with UV-vis-NIR spectrophotometry from 300 to 1000 nm (Thermo Scientific Evolution 201) and from 1100 to 2500 nm (Nicolet iS50R FT-IR) operating in transmission mode. Glass slides were used as a blank. Transmission was measured on three locations on each film and the average spectra are reported. Thin film surface roughness values were obtained by optical profilometry measurements (VKseries, Keyence). Optical properties of MXene colloidal solutions were measured in a concentration range between 0.01 and 0.04 mg mL<sup>-1</sup>. A 10 mm path length quartz cuvette filled with deionized water was used as a blank. The measured extinction was normalized to the path length (Ext/l), plotted versus concentration, and fit to the Beer Lambert equation, where the extinction coefficient was calculated from the slope of the linear trend. The analysis was conducted at 550 nm and from 200-1000 nm.

**Electrical Properties.** Electrical resistivity was measured using a Jandel cylindrical four-point probe with a ResTest Test Unit. The thickness of  $Mo_4VC_4$  MXene films was measured with a micrometer. The thickness of each film and the resistivity were measured at 10 places on each film and the average values are reported.

Temperature-dependence of resistivity and Hall measurements were performed in physical property measurement system (PPMS, Evercool II, Quantum Design). Free-standing MXene films were wired to the PPMS sample holder using silver wire and silver paint in 4-point and van de Pauw configurations. The resistance of the film

was recorded from 10 to 300 K with a heating/cooling rate of 4 K/min. Magnetoresistance (MR) and Hall resistance were measured at  $10~\mathrm{K}$  with a magnetic field up to  $5~\mathrm{T}$  applied perpendicular to the sample surface.

**Thermal Analysis.** The thermal stability of a  $\rm Mo_4VC_4$  film was studied by thermogravimetric analysis (SDT 650, TA Instruments) connected to a mass spectrometer (Discovery, TA Instruments). Freestanding MXene films with masses around 5 mg were packed in a 90  $\rm \mu L$  alumina pan and heated to 1500 °C at a constant heating rate of 10 °C/min under Ar atmosphere (100 mL/min). The furnace was purged with Ar gas (100 mL/min) for 1 h before the analysis to remove air residue.

Density Functional Theory Calculations. The Vienna Ab-Initio Simulation Package (VASP)<sup>79</sup> was used for all DFT calculations. Structural relaxations were performed with the Perdew-Burke-Ernzerhof (PBE)80 exchange-correlation functional and projector augmented wave (PAW) pseudopotentials,81 with a 520 eV planewave basis cutoff, a  $8 \times 8 \times 1$   $\Gamma$  centered k-point mesh for structural relaxations, and forces on each atom converged to below 10<sup>-2</sup> eV/Å. Electronic property calculations and total energies were converged to  $10^{-8}$  eV and a dense  $18 \times 18 \times 1\Gamma$  centered k-point mesh was used. 2  $\times$  2  $\times$  1 supercells (with 32 Mo atoms and 8 V atoms) were constructed to approximate disordered Mo<sub>4</sub>VC<sub>4</sub> solid-solutions. The Mo:V composition of 4:1 was kept fixed in all solid-solution calculations and 18 configurations were generated by randomly positioning the Mo and V atoms in the structure. Meshes were adjusted appropriately for 2 × 2 × 1 supercell solid-solution calculations. We have optimized the ordered and ground state disordered Mo<sub>4</sub>VAlC<sub>4</sub> structures with the PBEsol functional.<sup>82</sup> and c lattice constants change by less than 1% compared to calculations with PBE, and the solid-solutions are more favorable than the ordered configurations, regardless of functional choice. We have used reference energies from the Materials Project. The calculations for the stabilities of other M'4M"AlC4 MAX phases were limited to ordered phases where M" was sandwiched between two atomic layers of  $M^{\hat{\prime}}$  on both sides. Calculations of formation energies relative to the most stable unary phases provide trends in stability. However, the materials with negative formation energies could decompose into competing binary carbide, intermetallic, or other MAX phases that are more stable. Likewise, there may be materials with more stable solid-solution phases that have not been considered here. The work presented here is meant to provide trends in stability as a function of M element composition.

## **ASSOCIATED CONTENT**

# **S** Supporting Information

The Supporting Information is available free of charge at https://pubs.acs.org/doi/10.1021/acsnano.9b07708.

Additional results from the synthesis of  $Mo_4VAlC_4$ , including detailed synthesis procedure for washing and etching  $Mo_4VAlC_4$  and delamination of  $Mo_4VC_4$  MXene; optimization of the delamination process; TEM micrographs; high-resolution EDS line scan of the MAX phase structure; XPS results; overlaid version of the electrical resistivity; UV-vis-NIR extinction and transmission spectra; XRD and DFT exact values; sample crystal structures used for the DFT calculations. (PDF)

# **AUTHOR INFORMATION**

## **Corresponding Authors**

\*E-mail: gogotsi@drexel.edu. \*E-mail: banasori@iupui.edu.

ORCID ®

Grayson Deysher: 0000-0003-0482-8991

Christopher Eugene Shuck: 0000-0002-1274-8484

Kanit Hantanasirisakul: 0000-0002-4890-1444 Nathan C. Frey: 0000-0001-5291-6131 Alexandre C. Foucher: 0000-0001-5042-4002

Kathleen Maleski: 0000-0003-4032-7385 Eric A. Stach: 0000-0002-3366-2153 Babak Anasori: 0000-0002-1955-253X Yury Gogotsi: 0000-0001-9423-4032

#### **Notes**

The authors declare no competing financial interest.

#### **ACKNOWLEDGMENTS**

This work was funded by the U.S. Department of Energy (DOE), Office of Science, Office of Basic Energy Sciences, grant #DE-SC0018618. The authors would like to acknowledge the usage of the XRD, XPS, and SEM/EDS instrumentation provided by Drexel University Core Research Facility (CRF) and the University of Pennsylvania. C. Hatter (Drexel University) is acknowledged for providing additional TEM micrographs. Y. Yang and S. J. May (Drexel University) are acknowledged for helping with temperature-dependence of resistivity measurements. A. Fafarman (Drexel University) is acknowledged for access to the vis-NIR machine. V.B.S acknowledges support from the Army Research Office by contract W911NF-16-1-0447 and also grants CMMI-1727717 and EFMA-542879 from the National Science Foundation. N.C.F. was supported by the Department of Defense (DoD) through the National Defense Science & Engineering Graduate Fellowship (NDSEG) Program. This work was performed in part at the Singh Center for Nanotechnology at the University of Pennsylvania, a member of the National Nanotechnology Coordinated Infrastructure (NNCI) network, which is supported by the National Science Foundation (Grant NNCI-1542153). The authors gratefully acknowledge use of facilities and instrumentation supported by NSF through the University of Pennsylvania Materials Research Science and Engineering Center (MRSEC) (DMR-1720530). This research used resources of the Center for Functional Nanomaterials, which is a U.S. DOE Office of Science Facility, at Brookhaven National Laboratory under Contract No. DE-SC0012704. A.C.F. acknowledges support from Integrated Mesoscale Architectures for Sustainable Catalysis (IMASC), an Energy Frontier Research Center funded by the U.S. Department of Energy (DOE), Office of Science, Basic Energy Sciences (BES), under Award # DE-SC0012573.

## **REFERENCES**

- (1) Wang, Q. H.; Kalantar-Zadeh, K.; Kis, A.; Coleman, J. N.; Strano, M. S. Electronics and Optoelectronics of Two-Dimensional Transition Metal Dichalcogenides. *Nat. Nanotechnol.* **2012**, *7*, 699–712
- (2) Bonaccorso, F.; Sun, Z.; Hasan, T.; Ferrari, A. Graphene Photonics and Optoelectronics. *Nat. Photonics* **2010**, *4*, 611.
- (3) Shao, Y.; Wang, J.; Wu, H.; Liu, J.; Aksay, I. A.; Lin, Y. Graphene Based Electrochemical Sensors and Biosensors: A Review. *Electroanalysis* **2010**, 22, 1027–1036.
- (4) Watanabe, K.; Taniguchi, T.; Kanda, H. Direct-bandgap Properties and Evidence for Ultraviolet Lasing of Hexagonal Boron Nitride Single Crystal. *Nat. Mater.* **2004**, *3*, 404.
- (5) Naguib, M.; Kurtoglu, M.; Presser, V.; Lu, J.; Niu, J. J.; Heon, M.; Hultman, L.; Gogotsi, Y.; Barsoum, M. W. Two-Dimensional Nanocrystals Produced by Exfoliation of Ti<sub>3</sub>AlC<sub>2</sub>. *Adv. Mater.* **2011**, 23, 4248–4253.

(6) Anasori, B.; Lukatskaya, M. R.; Gogotsi, Y. 2D Metal Carbides and Nitrides (MXenes) for Energy Storage. *Nat. Rev. Mater.* **2017**, *2*, 16098.

- (7) Tao, Q.; Dahlqvist, M.; Lu, J.; Kota, S.; Meshkian, R.; Halim, J.; Palisaitis, J.; Hultman, L.; Barsoum, M. W.; Persson, P. O. Two-Dimensional Mo<sub>1.33</sub>C MXene with Divacancy Ordering Prepared from Parent 3D Laminate with In-Plane Chemical Ordering. *Nat. Commun.* **2017**, *8*, 14949.
- (8) Yang, J.; Naguib, M.; Ghidiu, M.; Pan, L. M.; Gu, J.; Nanda, J.; Halim, J.; Gogotsi, Y.; Barsoum, M. W. Two-Dimensional Nb-Based M<sub>4</sub>C<sub>3</sub> Solid Solutions (MXenes). *J. Am. Ceram. Soc.* **2016**, *99*, 660–665.
- (9) Lukatskaya, M. R.; Mashtalir, O.; Ren, C. E.; Dall'Agnese, Y.; Rozier, P.; Taberna, P. L.; Naguib, M.; Simon, P.; Barsoum, M. W.; Gogotsi, Y. Cation Intercalation and High Volumetric Capacitance of Two-Dimensional Titanium Carbide. *Science* 2013, 341, 1502–1505.
- (10) Huang, K.; Li, Z.; Lin, J.; Han, G.; Huang, P. Two-Dimensional Transition Metal Carbides and Nitrides (MXenes) for Biomedical Applications. *Chem. Soc. Rev.* **2018**, *47*, 5109–5124.
- (11) Hantanasirisakul, K.; Zhao, M. Q.; Urbankowski, P.; Halim, J.; Anasori, B.; Kota, S.; Ren, C. E.; Barsoum, M. W.; Gogotsi, Y. Fabrication of Ti<sub>3</sub>C<sub>2</sub>T<sub>x</sub> MXene Transparent Thin Films with Tunable Optoelectronic Properties. *Adv. Electron. Mater.* **2016**, *2*, 1600050.
- (12) Salles, P.; Pinto, D.; Hantanasirisakul, K.; Maleski, K.; Shuck, C. E.; Gogotsi, Y. Electrochromic Effect in Titanium Carbide MXene Thin Films Produced by Dip-Coating. *Adv. Funct. Mater.* **2019**, 29, 1809223.
- (13) Alhabeb, M.; Maleski, K.; Anasori, B.; Lelyukh, P.; Clark, L.; Sin, S.; Gogotsi, Y. Guidelines for Synthesis and Processing of Two-Dimensional Titanium Carbide (Ti<sub>3</sub>C<sub>2</sub>T<sub>x</sub> MXene). *Chem. Mater.* **2017**, 29, 7633–7644.
- (14) Dillon, A. D.; Ghidiu, M. J.; Krick, A. L.; Griggs, J.; May, S. J.; Gogotsi, Y.; Barsoum, M. W.; Fafarman, A. T. Highly Conductive Optical Quality Solution-Processed Films of 2D Titanium Carbide. *Adv. Funct. Mater.* **2016**, 26, 4162–4168.
- (15) Naguib, M.; Halim, J.; Lu, J.; Cook, K. M.; Hultman, L.; Gogotsi, Y.; Barsoum, M. W. New Two-Dimensional Niobium and Vanadium Carbides as Promising Materials for Li-Ion Batteries. *J. Am. Chem. Soc.* **2013**, *135*, 15966–15969.
- (16) Gao, G.; O'Mullane, A. P.; Du, A. 2D MXenes: A New Family of Promising Catalysts for the Hydrogen Evolution Reaction. *ACS Catal.* **2017**, *7*, 494–500.
- (17) Ran, J.; Gao, G.; Li, F.-T.; Ma, T.-Y.; Du, A.; Qiao, S.-Z. Ti<sub>3</sub>C<sub>2</sub> MXene Co-Catalyst on Metal Sulfide Photo-Absorbers for Enhanced Visible-Light Photocatalytic Hydrogen Production. *Nat. Commun.* **2017**, *8*, 13907.
- (18) Sarycheva, A.; Polemi, A.; Liu, Y.; Dandekar, K.; Anasori, B.; Gogotsi, Y. 2D Titanium Carbide (MXene) for Wireless Communication. *Sci. Adv.* **2018**, *4*, No. eaau0920.
- (19) Shahzad, F.; Alhabeb, M.; Hatter, C. B.; Anasori, B.; Hong, S. M.; Koo, C. M.; Gogotsi, Y. Electromagnetic Interference Shielding with 2D Transition Metal Carbides (MXenes). *Science* **2016**, 353, 1137–1140.
- (20) Han, M.; Yin, X.; Hantanasirisakul, K.; Li, X.; Iqbal, A.; Hatter, C. B.; Anasori, B.; Koo, C. M.; Torita, T.; Soda, Y. Anisotropic MXene Aerogels with a Mechanically Tunable Ratio of Electromagnetic Wave Reflection to Absorption. *Adv. Opt. Mater.* **2019**, *7*, 1900267.
- (21) Kim, S. J.; Koh, H.-J.; Ren, C. E.; Kwon, O.; Maleski, K.; Cho, S.-Y.; Anasori, B.; Kim, C.-K.; Choi, Y.-K.; Kim, J. Metallic  ${\rm Ti}_3{\rm C}_2{\rm T}_x$  MXene Gas Sensors with Ultrahigh Signal-to-Noise Ratio. *ACS Nano* **2018**, *12*, 986–993.
- (22) Hantanasirisakul, K.; Gogotsi, Y. Electronic and Optical Properties of 2D Transition Metal Carbides and Nitrides (MXenes). *Adv. Mater.* **2018**, *30*, 1804779.
- (23) Hart, J. L.; Hantanasirisakul, K.; Lang, A. C.; Anasori, B.; Pinto, D.; Pivak, Y.; van Omme, J. T.; May, S. J.; Gogotsi, Y.; Taheri, M. L. Control of MXenes' Electronic Properties through Termination and Intercalation. *Nat. Commun.* **2019**, *10*, 522.

- (24) Shuck, C. E.; Han, M.; Maleski, K.; Hantanasirisakul, K.; Kim, S. J.; Choi, J.; Reil, W.; Gogotsi, Y. Effect of Ti<sub>3</sub>AlC<sub>2</sub> MAX Phase on Structure and Properties of Resultant Ti<sub>3</sub>C<sub>2</sub>T<sub>x</sub> MXene. *ACS Appl. Nano Mater.* **2019**, *2*, 3368–3376.
- (25) Hantanasirisakul, K.; Alhabeb, M.; Lipatov, A.; Maleski, K.; Anasori, B.; Salles, P.; Ieosakulrat, C.; Pakawatpanurut, P.; Sinitskii, A.; May, S. J. Effects of Synthesis and Processing on Optoelectronic Properties of Titanium Carbonitride MXene. *Chem. Mater.* **2019**, *31*, 2941–2951.
- (26) Seredych, M.; Shuck, C. E.; Pinto, D.; Alhabeb, M.; Precetti, E.; Deysher, G.; Anasori, B.; Kurra, N.; Gogotsi, Y. High-Temperature Behavior and Surface Chemistry of Carbide MXenes Studied by Thermal Analysis. *Chem. Mater.* **2019**, *31*, 3324–3332.
- (27) Kim, H.; Anasori, B.; Gogotsi, Y.; Alshareef, H. N. Thermoelectric Properties of Two-Dimensional Molybdenum-Based MXenes. *Chem. Mater.* **2017**, 29, 6472–6479.
- (28) Bao, W.; Shuck, C. E.; Zhang, W.; Guo, X.; Gogotsi, Y.; Wang, G. Boosting Performance of Na–S Batteries Using Sulfur-Doped  ${\rm Ti}_3{\rm C}_2{\rm T}_x$  MXene Nanosheets with a Strong Affinity to Sodium Polysulfides. *ACS Nano* **2019**, *13*, 11500–11509.
- (29) Soundiraraju, B.; George, B. K. Two-Dimensional Titanium Nitride (Ti<sub>2</sub>N) MXene: Synthesis, Characterization, and Potential Application as Surface-Enhanced Raman Scattering Substrate. *ACS Nano* **2017**, *11*, 8892–8900.
- (30) Urbankowski, P.; Anasori, B.; Hantanasirisakul, K.; Yang, L.; Zhang, L.; Haines, B.; May, S. J.; Billinge, S. J.; Gogotsi, Y. 2D Molybdenum and Vanadium Nitrides Synthesized by Ammoniation of 2D Transition Metal Carbides (MXenes). *Nanoscale* **2017**, *9*, 17722–17730.
- (31) Kurtoglu, M.; Naguib, M.; Gogotsi, Y.; Barsoum, M. W. First Principles Study of Two-Dimensional Early Transition Metal Carbides. MRS Commun. 2012, 2, 133–137.
- (32) Meshkian, R.; Näslund, L.-Å.; Halim, J.; Lu, J.; Barsoum, M. W.; Rosen, J. Synthesis of Two-Dimensional Molybdenum Carbide, Mo<sub>2</sub>C, from the Gallium Based Atomic Laminate Mo<sub>2</sub>Ga<sub>2</sub>C. *Scr. Mater.* **2015**, *108*, 147–150.
- (33) Abdelmalak, M. N. MXenes: A New Family of Two-Dimensional Materials and its Application as Electrodes for Li-Ion Batteries; Drexel University: Philadelphia, 2014.
- (34) Meshkian, R.; Dahlqvist, M.; Lu, J.; Wickman, B.; Halim, J.; Thörnberg, J.; Tao, Q.; Li, S.; Intikhab, S.; Snyder, J. W-Based Atomic Laminates and Their 2D Derivative W<sub>1,33</sub>C MXene with Vacancy Ordering. *Adv. Mater.* **2018**, *30*, 1706409.
- (35) Halim, J.; Palisaitis, J.; Lu, J.; Thörnberg, J.; Moon, E.; Precner, M.; Eklund, P.; Persson, P. Å.; Barsoum, M.; Rosen, J. Synthesis of Two-Dimensional Nb<sub>1,33</sub>C (MXene) with Randomly Distributed Vacancies by Etching of the Quaternary Solid Solution (Nb<sub>2/3</sub>Sc<sub>1/3</sub>)<sub>2</sub>AlC MAX Phase. ACS Appl. Nano Mater. **2018**, 1, 2455–2460.
- (36) Persson, I.; El Ghazaly, A.; Tao, Q.; Halim, J.; Kota, S.; Darakchieva, V.; Palisaitis, J.; Barsoum, M. W.; Rosen, J.; Persson, P. O. Tailoring Structure, Composition, and Energy Storage Properties of MXenes from Selective Etching of In-Plane, Chemically Ordered MAX Phases. *Small* **2018**, *14*, 1703676.
- (37) Naguib, M.; Mashtalir, O.; Carle, J.; Presser, V.; Lu, J.; Hultman, L.; Gogotsi, Y.; Barsoum, M. W. Two-Dimensional Transition Metal Carbides. *ACS Nano* **2012**, *6*, 1322–1331.
- (38) Zhou, J.; Zha, X.; Zhou, X.; Chen, F.; Gao, G.; Wang, S.; Shen, C.; Chen, T.; Zhi, C.; Eklund, P. Synthesis and Electrochemical Properties of Two-Dimensional Hafnium Carbide. *ACS Nano* **2017**, *11*, 3841–3850.
- (39) Zhou, J.; Zha, X.; Chen, F. Y.; Ye, Q.; Eklund, P.; Du, S.; Huang, Q. A Two-Dimensional Zirconium Carbide by Selective Etching of  $Al_3C_3$  from Nanolaminated  $Zr_3Al_3C_5$ . Angew. Chem. **2016**, 128, 5092–5097.
- (40) Anasori, B.; Xie, Y.; Beidaghi, M.; Lu, J.; Hosler, B. C.; Hultman, L.; Kent, P. R.; Gogotsi, Y.; Barsoum, M. W. Two-Dimensional, Ordered, Double Transition Metals Carbides (MXenes). ACS Nano 2015, 9, 9507–9516.

(41) Meshkian, R.; Tao, Q.; Dahlqvist, M.; Lu, J.; Hultman, L.; Rosen, J. Theoretical Stability and Materials Synthesis of a Chemically Ordered MAX Phase, Mo<sub>2</sub>ScAlC<sub>2</sub>, and Its Two-Dimensional Derivate Mo<sub>2</sub>ScC<sub>2</sub> MXene. *Acta Mater.* **2017**, *125*, 476–480.

- (42) Urbankowski, P.; Anasori, B.; Makaryan, T.; Er, D.; Kota, S.; Walsh, P. L.; Zhao, M.; Shenoy, V. B.; Barsoum, M. W.; Gogotsi, Y. Synthesis of Two-Dimensional Titanium Nitride Ti<sub>4</sub>N<sub>3</sub> (MXene). *Nanoscale* **2016**, *8*, 11385–11391.
- (43) Tran, M. H.; Schäfer, T.; Shahraei, A.; Dürrschnabel, M.; Molina-Luna, L.; Kramm, U. I.; Birkel, C. S. Adding a New Member to the MXene Family: Synthesis, Structure, and Electrocatalytic Activity for the Hydrogen Evolution Reaction of V<sub>4</sub>C<sub>3</sub>T<sub>x</sub>. ACS Appl. Energy Mater. 2018, 1, 3908–3914.
- (44) Ghidiu, M.; Naguib, M.; Shi, C.; Mashtalir, O.; Pan, L.; Zhang, B.; Yang, J.; Gogotsi, Y.; Billinge, S. J.; Barsoum, M. W. Synthesis and Characterization of Two-Dimensional Nb<sub>4</sub>C<sub>3</sub> (MXene). *Chem. Commun.* **2014**, *50*, 9517–9520.
- (45) Tan, T. L.; Jin, H. M.; Sullivan, M. B.; Anasori, B.; Gogotsi, Y. High-Throughput Survey of Ordering Configurations in MXene Alloys Across Compositions and Temperatures. *ACS Nano* **2017**, *11*, 4407–4418.
- (46) Khazaei, M.; Ranjbar, A.; Esfarjani, K.; Bogdanovski, D.; Dronskowski, R.; Yunoki, S. Insights into Exfoliation Possibility of MAX Phases to MXenes. *Phys. Chem. Chem. Phys.* **2018**, 20, 8579–8592.
- (47) Alhabeb, M.; Maleski, K.; Mathis, T. S.; Sarycheva, A.; Hatter, C. B.; Uzun, S.; Levitt, A.; Gogotsi, Y. Selective Etching of Silicon from Ti<sub>3</sub>SiC<sub>2</sub> (MAX) to Obtain 2D Titanium Carbide (MXene). *Angew. Chem., Int. Ed.* **2018**, *57*, 5444–5448.
- (48) Lin, Z.; Zhuo, M.; Zhou, Y.; Li, M.; Wang, J. Microstructures and Theoretical Bulk Modulus of Layered Ternary Tantalum Aluminum Carbides. J. Am. Ceram. Soc. 2006, 89, 3765–3769.
- (49) Zhang, J.; Liu, B.; Wang, J.; Zhou, Y. Low-Temperature Instability of Ti<sub>2</sub>SnC: A Combined Transmission Electron Microscopy, Differential Scanning Calorimetry, and X-Ray Diffraction Investigations. *J. Mater. Res.* **2009**, *24*, 39–49.
- (50) Zheng, L.; Wang, J.; Lu, X.; Li, F.; Wang, J.; Zhou, Y. (Ti<sub>0.5</sub>Nb<sub>0.5</sub>)<sub>5</sub>AlC<sub>4</sub>: A New-Layered Compound Belonging to MAX Phases. *J. Am. Ceram. Soc.* **2010**, 93, 3068–3071.
- (51) Xie, Y.; Kent, P. Hybrid Density Functional Study of Structural and Electronic Properties of Functionalized  $Ti_{n+1}X_n$  (X= C, N) Monolayers. *Phys. Rev. B: Condens. Matter Mater. Phys.* **2013**, 87, 235441.
- (52) Zhou, Y.; Sun, Z. Electronic Structure and Bonding Properties of Layered Machinable Ti<sub>2</sub>AlC and Ti<sub>2</sub>AlN ceramics. *Phys. Rev. B: Condens. Matter Mater. Phys.* **2000**, *61*, 12570.
- (53) Tzenov, N. V.; Barsoum, M. W. Synthesis and Characterization of Ti<sub>3</sub>AlC<sub>2</sub>. J. Am. Ceram. Soc. **2000**, 83, 825–832.
- (54) Lin, Z.; Zhuo, M.; Zhou, Y.; Li, M.; Wang, J. Structural Characterization of a New Layered-Ternary Ta<sub>4</sub>AlC<sub>3</sub> Ceramic. *J. Mater. Res.* **2006**, 21, 2587–2592.
- (55) Lipatov, A.; Lu, H.; Alhabeb, M.; Anasori, B.; Gruverman, A.; Gogotsi, Y.; Sinitskii, A. Elastic Properties of 2D Ti<sub>3</sub>C<sub>2</sub>T<sub>x</sub> MXene Monolayers and Bilayers. *Sci. Adv.* **2018**, *4*, No. eaat0491.
- (56) Newbury, D. E. Standardless Quantitative Electron-Excited X-Ray Microanalysis by Energy-Dispersive Spectrometry: What is Its Proper Role? *Microsc. Microanal.* **1998**, *4*, 585–597.
- (57) Naguib, M.; Unocic, R. R.; Armstrong, B. L.; Nanda, J. Large-Scale Delamination of Multi-Layers Transition Metal Carbides and Carbonitrides "MXenes. *Dalton Trans* **2015**, *44*, 9353–9358.
- (58) Anasori, B.; Shi, C.; Moon, E. J.; Xie, Y.; Voigt, C. A.; Kent, P. R.; May, S. J.; Billinge, S. J.; Barsoum, M. W.; Gogotsi, Y. Control of Electronic Properties of 2D Carbides (MXenes) by Manipulating Their Transition Metal Layers. *Nanoscale Horiz* **2016**, *1*, 227–234.
- (59) Halim, J.; Kota, S.; Lukatskaya, M. R.; Naguib, M.; Zhao, M. Q.; Moon, E. J.; Pitock, J.; Nanda, J.; May, S. J.; Gogotsi, Y. Synthesis and Characterization of 2D Molybdenum Carbide (MXene). *Adv. Funct. Mater.* **2016**, *26*, 3118–3127.

(60) Halim, J.; Cook, K. M.; Naguib, M.; Eklund, P.; Gogotsi, Y.; Rosen, J.; Barsoum, M. W. X-Ray Photoelectron Spectroscopy of Select Multi-Layered Transition Metal Carbides (MXenes). *Appl. Surf. Sci.* **2016**, 362, 406–417.

- (61) Seh, Z. W.; Fredrickson, K. D.; Anasori, B.; Kibsgaard, J.; Strickler, A. L.; Lukatskaya, M. R.; Gogotsi, Y.; Jaramillo, T. F.; Vojvodic, A. Two-Dimensional Molybdenum Carbide (MXene) as an Efficient Electrocatalyst for Hydrogen Evolution. *ACS Energy Lett.* **2016**, *1*, 589–594.
- (62) Etzkorn, J.; Ade, M.; Hillebrecht, H.  $V_2AlC$ ,  $V_4AlC_{3-x}$  ( $x\approx 0.31$ ), and  $V_{12}Al_3C_8$ : Synthesis, Crystal Growth, Structure, and Superstructure. *Inorg. Chem.* **2007**, *46*, 7646–7653.
- (63) Dahlqvist, M.; Alling, B.; Rosén, J. Stability Trends of MAX Phases from First Principles. *Phys. Rev. B: Condens. Matter Mater. Phys.* **2010**, *81*, 220102.
- (64) Zeiger, M.; Ariyanto, T.; Krüner, B.; Peter, N. J.; Fleischmann, S.; Etzold, B. J.; Presser, V. Vanadium Pentoxide/carbide-derived Carbon Core—Shell Hybrid Particles for High Performance Electrochemical Energy Storage. *J. Mater. Chem. A* **2016**, *4*, 18899—18909.
- (65) Li, T.; Luo, W.; Kitadai, H.; Wang, X.; Ling, X. Probing the Domain Architecture in 2D Alpha-Mo<sub>2</sub>C *via* Polarized Raman. *Adv. Mater.* **2019**, *31*, 1807160.
- (66) Sun, Y.; Cui, H.; Gong, L.; Chen, J.; She, J.; Ma, Y.; Shen, P.; Wang, C. Carbon-in-Al<sub>4</sub>C<sub>3</sub> Nanowire Superstructures for Field Emitters. *ACS Nano* **2011**, *5*, 932–941.
- (67) Hu, T.; Hu, M.; Li, Z.; Zhang, H.; Zhang, C.; Wang, J.; Wang, X. Covalency-Dependent Vibrational Dynamics in Two-Dimensional Titanium Carbides. *J. Phys. Chem. A* **2015**, *119*, 12977–12984.
- (68) Hu, T.; Wang, J.; Zhang, H.; Li, Z.; Hu, M.; Wang, X. Vibrational Properties of Ti<sub>3</sub>C<sub>2</sub> and Ti<sub>3</sub>C<sub>2</sub>T<sub>2</sub> (T= O, F, OH) Monosheets by First-Principles Calculations: A Comparative Study. *Phys. Chem. Chem. Phys.* **2015**, *17*, 9997–10003.
- (69) Zhao, S.; Meng, X.; Zhu, K.; Du, F.; Chen, G.; Wei, Y.; Gogotsi, Y.; Gao, Y. Li-Ion Uptake and Increase in Interlayer Spacing of Nb<sub>4</sub>C<sub>3</sub> MXene. *Energy Storage Mater.* **2017**, *8*, 42–48.
- (70) Gouadec, G.; Colomban, P. Raman Spectroscopy of Nanomaterials: How Spectra Relate to Disorder, Particle Size and Mechanical Properties. *Prog. Cryst. Growth Charact. Mater.* **2007**, *53*, 1–56.
- (71) Yang, S.; Evmiridis, N. Synthesis of Omega Zeolite Without Use of Tetramethylammonium (TMA) Ions. In *Studies in Surfuce Science and Catalysis*, Weitkamp, J.; Karge, H. G.; Pfeifer, H.; Hölderich, W., Eds.; Elsevier: New York, 1994; Vol. 84, pp 155–162.
- (72) Ouisse, T.; Barsoum, M. W. Magnetotransport in the MAX Phases and Their 2D Derivatives: MXenes. *Mater. Res. Lett.* **2017**, *5*, 365–378.
- (73) Kasap, S. O. Principles of Electronic Materials and Devices; McGraw-Hill: New York, 2006; Vol. 2.
- (74) Ying, G.; Kota, S.; Dillon, A. D.; Fafarman, A. T.; Barsoum, M. W. Conductive Transparent  $V_2CT_x$  (MXene) Films. *FlatChem.* **2018**, 8, 25–30.
- (75) Ashton, M.; Hennig, R. G.; Broderick, S. R.; Rajan, K.; Sinnott, S. B. Computational Discovery of Stable M<sub>2</sub>AX Phases. *Phys. Rev. B: Condens. Matter Mater. Phys.* **2016**, *94*, 054116.
- (76) Van De Walle, A.; Asta, M.; Ceder, G. The Alloy Theoretic Automated Toolkit: A User Guide. *CALPHAD: Comput. Coupling Phase Diagrams Thermochem.* **2002**, 26, 539–553.
- (77) Sokol, M.; Natu, V.; Kota, S.; Barsoum, M. W. On the Chemical Diversity of the MAX Phases. *Trends in Chem.* **2019**, *1*, 210–223.
- (78) Frey, N. C.; Wang, J.; Vega Bellido, G. I. n.; Anasori, B.; Gogotsi, Y.; Shenoy, V. B. Prediction of Synthesis of 2D Metal Carbides and Nitrides (MXenes) and Their Precursors with Positive and Unlabeled Machine Learning. ACS Nano 2019, 13, 3031–3041.
- (79) Kresse, G.; Furthmüller, J. Efficient Iterative Schemes for *Ab Initio* Total-Energy Calculations Using a Plane-Wave Basis Set. *Phys. Rev. B: Condens. Matter Mater. Phys.* **1996**, 54, 11169.
- (80) Perdew, J. P.; Burke, K.; Ernzerhof, M. Generalized Gradient Approximation Made Simple. *Phys. Rev. Lett.* **1996**, 77, 3865.

(81) Kresse, G.; Joubert, D. From Ultrasoft Pseudopotentials to the Projector Augmented-Wave Method. *Phys. Rev. B: Condens. Matter Mater. Phys.* **1999**, *59*, 1758.

(82) Perdew, J. P.; Ruzsinszky, A.; Csonka, G. I.; Vydrov, O. A.; Scuseria, G. E.; Constantin, L. A.; Zhou, X.; Burke, K. Restoring the Density-Gradient Expansion for Exchange in Solids and Surfaces. *Phys. Rev. Lett.* **2008**, *100*, 136406.